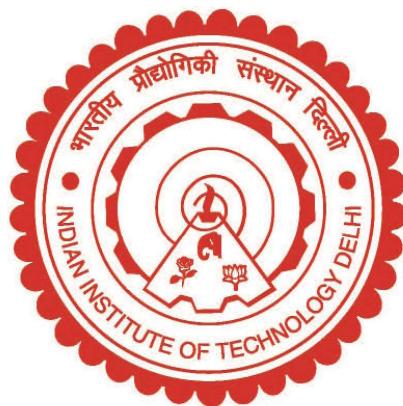


**SPIN-TO-CHARGE CONVERSION AND SPIN-ORBIT TORQUE  
IN HETEROSTRUCTURES UTILIZING VAN DER WAALS  
MATERIALS AND NON-COLLINEAR ANTIFERROMAGNETS**

**HIMANSHU**



Department of Physics

**INDIAN INSTITUTE OF TECHNOLOGY DELHI**

**May 2024**

© Indian Institute of Technology Delhi (IITD), New Delhi, 2024

**SPIN-TO-CHARGE CONVERSION AND SPIN-ORBIT TORQUE  
IN HETEROSTRUCTURES UTILIZING VAN DER WAALS  
MATERIALS AND NON-COLLINEAR ANTIFERROMAGNETS**

by

**HIMANSHU**

Department of Physics

Submitted

in fulfillment of the requirements for the degree of Doctor of Philosophy to the



**INDIAN INSTITUTE OF TECHNOLOGY DELHI**

**May 2024**

## Certificate

This is to certify that the thesis entitled, **Spin-to-Charge Conversion and Spin-Orbit Torque in Heterostructures utilizing Van der Waals Materials and Non-Collinear Antiferromagnets**, is being submitted by **Mr. Himanshu** to the Department of Physics, Indian Institute of Technology Delhi, for the award of the degree of **Doctor of Philosophy**. This work is a record of bonafide research conducted by him. He has worked under my supervision and guidance and has fulfilled all the requirements for the submission of this thesis. In my opinion, the work has reached the requisite standard.

The results presented in this thesis have not been submitted, either in part or in full, to any other University or Institute for the award of any degree or diploma.

---

**Prof. P. K. Muduli**

Professor

Department of Physics

Indian Institute of Technology Delhi

New Delhi - 110016

India,

Date:



## Acknowledgements

This work represents the culmination of my unforgettable five-year Ph.D. journey. Successful completion of this research would not have been possible without the invaluable contributions of many individuals.

First and foremost, I express my sincere gratitude to my Ph.D. supervisor, Prof. Pranaba Kishor Muduli, for his unwavering support and guidance. I am thankful for the opportunity to work on this fascinating research topic and for the continuous flow of innovative ideas he provided throughout this journey. His logical thinking and profound scientific insight significantly elevated the quality of the research presented in this thesis. I appreciate his willingness to dedicate time from his busy schedule for our discussions, which greatly enhanced my knowledge and curiosity about the latest developments in our field. I am also grateful for his encouragement and support in my participation in numerous online and offline conferences, allowing me to interact with peers and gain insights into their work.

I extend my gratitude to the members of the SRC committee, Prof. Santanu Ghosh, Prof. Rajendra Dhaka, and Prof. Samaresh Das, for their consistent feedback, valuable insights, and engaging discussions during my Ph.D. tenure.

I express my gratitude to the Physics Department, High-Performance Computing (HPC), Nanoscale Research Facility (NRF), and Central Research Facility (CRF) at IIT Delhi for providing the necessary infrastructure for sample preparation, device fabrication, characterization, software, and computing. I would also like to acknowledge the Council of Scientific and Industrial Research (CSIR) for their financial support throughout my research journey.

I thank all my senior labmates for fostering a welcoming environment since the beginning of my research journey. I want to give special thanks to Dr. Niru Chowdhury and Dr. Akash Kumar for their unwavering help and support during our daily experiments and scientific discussions. Their profound understanding and experience in sample growth, experimental measurements, and analysis have been instrumental in reducing errors and enriching my comprehension of the physics encapsulated in this thesis. I would also like to express my appreciation to Dr. Naveen Sisodia for teaching me the fundamentals of micromagnetic simulations during the COVID-19 lockdown. This not only helped me use my time efficiently but also enhanced my understanding of spintronics phenomena. Dr. Sheetal Dewan's guidance on operating the PLD system and her assistance during sample growth and characterization have been invaluable. Dr. Kacho Imtiyaz Ali Khan deserves

my thanks for his contributions to sample growth, XRD measurements, and engaging discussions throughout my Ph.D. tenure. I am grateful to Pankhuri Gupta for her assistance with ST-FMR measurements, device fabrication, and insightful discussions. I am thankful to Namrata Bansal for her continuous support and insightful discussions on the DMI work and writing manuscripts. My appreciation also goes to Ram Singh Yadav and Rekha Agarwal for their continuous help, support, and discussions. I would like to acknowledge and thank all my junior colleagues: Richa Mudgal, Neha Garg, Deeksha Gupta, Azminul Jaman, Upasna Bordoloi, Ujjawal Rathore, Uzer Ahmad, Nidhi Kandwal, Alen John, Jasmeen Virk, Aman Saxena, and Vaishali Yadav for their contributions and thoughtful discussions.

I am deeply grateful to my friends, including Vikrant Giri, Aditi Mehta, Nandini Patel, Sumit Sharma, Sachin Sharma, and Nomendra Tomar. They have played an instrumental role in making my Ph.D. journey truly memorable. The moments we have shared will be cherished for the rest of my life.

Finally, I would like to extend my heartfelt gratitude to my parents and extended family. Their continuous support, unconditional love, and unwavering encouragement have been the driving force behind my journey. None of this would have been possible without their blessings and enduring support. I owe my presence here to my parent's sacrifices and tireless efforts in paving the way for a brighter future. They have consistently provided me with support and invaluable wisdom throughout my life.

*This thesis is dedicated to my parents.*

Himanshu

## Abstract

This thesis explores spin-to-charge conversion and spin-orbit torques (SOTs) in two novel classes of quantum materials that are interesting from both fundamental and applied perspectives. The focus is on two significant classes of materials: van der Waals materials and non-collinear antiferromagnets. These quantum materials exhibit unique spin-dependent characteristics, which can be exploited to obtain a substantial tunable spin-charge interconversion efficiency and generate unconventional spin currents. These properties make them highly suitable for applications requiring spin-charge conversion and SOT.

Firstly, large-area van der Waals materials are explored for spin-to-charge conversion and SOT. A systematic study of spin-to-charge conversion at the interface of  $\text{Ni}_{80}\text{Fe}_{20}$  and large area monolayer (ML) transition metal dichalcogenides (TMDs) -  $\text{MoS}_2$ ,  $\text{MoSe}_2$ ,  $\text{WS}_2$ , and  $\text{WSe}_2$  - is conducted. Large spin-to-charge conversion is observed in these systems, with efficiencies scaling with the spin-orbit coupling of the ML TMD layer, consistent with the inverse Rashba-Edelstein effect. The efficiency of W-based TMDs exceeds that of Mo-based TMDs. Subsequently, high-quality two-dimensional growth of few-layer SnS on CMOS-compatible Si/SiO<sub>2</sub> substrates using the pulsed laser deposition (PLD) technique is demonstrated. Spin-torque ferromagnetic resonance (STFMR) experiments on SnS(1.3 nm)/ $\text{Ni}_{80}\text{Fe}_{20}$ (8 nm) devices reveal evidence of an unconventional SOT. The growth of the  $\alpha$ -phase of another van der Waals material, GeTe, on Si(111) substrates is optimized using PLD. Angle-resolved STFMR reveals a substantial in-plane damping-like torque in GeTe/ $\text{Ni}_{80}\text{Fe}_{20}$  devices. The calculated damping-like spin torque conductivity is  $(-1.25 \pm 0.11) \times 10^5 \hbar/2e \Omega^{-1} \text{m}^{-1}$ , marking one of the highest reported values for van der Waals materials. These results underscore the potential of van der Waals materials for highly efficient spintronics devices.

Subsequently, we focus on the non-collinear antiferromagnet  $\text{Mn}_3\text{Sn}$ , a magnetic Weyl semimetal with great potential for efficient memory devices. We grow high-quality epitaxial  $c$ -plane  $\text{Mn}_3\text{Sn}$  on  $\text{Al}_2\text{O}_3$  substrate using Ru as the seed layer. Using spin pumping-induced inverse spin Hall effect measurements on  $c$ -plane epitaxial  $\text{Mn}_3\text{Sn}/\text{Ni}_{80}\text{Fe}_{20}$ , spin-diffusion length ( $\lambda_{\text{Mn}_3\text{Sn}}$ ), and spin Hall conductivity ( $\sigma_{\text{SH}}$ ) of  $\text{Mn}_3\text{Sn}$  thin films are measured to be  $0.42 \pm 0.04$  nm and  $(-1.40 \pm 0.07) \times 10^5 \hbar/2e \Omega^{-1} \text{m}^{-1}$ , respectively. While  $\lambda_{\text{Mn}_3\text{Sn}}$  is consistent with earlier studies,  $\sigma_{\text{SH}}$  is an order of magnitude higher and of the opposite sign, which is explained by the shift in the Fermi level. The growth of  $a$ -plane and polycrystalline  $\text{Mn}_3\text{Sn}$  is optimized, providing an opportunity to compare spin-charge conversion in different crystalline orientations. The spin Hall angle for  $c$ -plane and  $a$ -plane orientations is nearly equal but opposite signs, possibly due to different orientations of

their kagome plane. Additionally, a systematic STFM study reveals the presence of out-of-plane polarized spin current ( $p_z$ ) in  $\text{Mn}_3\text{Sn}/\text{Py}$  devices. The  $p_z$  in  $c$ -plane  $\text{Mn}_3\text{Sn}$  is anisotropic, while it is isotropic in  $a$ -plane  $\text{Mn}_3\text{Sn}$ . Unconventional damping-like and field-like torque in  $a$ -plane and polycrystalline  $\text{Mn}_3\text{Sn}$  are observed for the first time. These results position non-collinear antiferromagnet  $\text{Mn}_3\text{Sn}$  as a promising candidate for next-generation spintronics devices.

## सारांश

यह शोध प्रबंध दो नए प्रकार की क्वांटम सामग्रियों में स्पिन-से-चार्ज रूपांतरण और स्पिन-ऑर्बिट टॉर्क्स (SOTs) का अन्वेषण करता है, जो मौलिक और अनुप्रयुक्त दोनों दृष्टिकोणों से दिलचस्प हैं। ध्यान दो महत्वपूर्ण प्रकार की सामग्रियों पर है: वैन डर वाल्स सामग्री और गैर-सरेखित प्रतिचुंबक। इन क्वांटम सामग्रियों में अद्वितीय स्पिन-निर्भर विशेषताएँ होती हैं, जिनका उपयोग उच्चतम समायोज्य स्पिन-चार्ज इंटरकन्वर्जन दक्षता प्राप्त करने और असामान्य स्पिन धाराओं को उत्पन्न करने के लिए किया जा सकता है। ये गुण उन्हें स्पिन-चार्ज रूपांतरण और SOT की आवश्यकता वाले अनुप्रयोगों के लिए अत्यधिक उपयुक्त बनाते हैं।

पहले, वैन डर वाल्स सामग्रियों के बड़े क्षेत्र को स्पिन-से-चार्ज रूपांतरण और SOT के लिए अन्वेषित किया जाता है।  $\text{Ni}_{80}\text{Fe}_{20}$  और बड़े क्षेत्र मोनोलायर (ML) ट्रांज़िशन मेटल डायकैल्कोजेनाइड्स (TMDs) -  $\text{MoS}_2$ ,  $\text{MoSe}_2$ ,  $\text{WS}_2$ , और  $\text{WSe}_2$  - के इंटरफेस पर स्पिन-से-चार्ज रूपांतरण का एक व्यवस्थित अध्ययन किया जाता है। इन प्रणालियों में बड़े स्पिन-से-चार्ज रूपांतरण देखे जाते हैं, जिनकी दक्षता ML TMD परत की स्पिन-ऑर्बिट कपलिंग के अनुसार स्केल होती है, जो इनवर्स राशबा-एडलस्टीन प्रभाव के अनुरूप है। W-आधारित TMDs की दक्षता Mo-आधारित TMDs से अधिक होती है। इसके बाद, PLD तकनीक का उपयोग करके CMOS-संगत Si/SiO<sub>2</sub> सबस्ट्रेट पर कुछ-परत SnS की उच्च-गुणवत्ता वाली द्वि-आयामी वृद्धि का प्रदर्शन किया जाता है। SnS(1.3 nm)/  $\text{Ni}_{80}\text{Fe}_{20}$ (8 nm) उपकरणों पर किए गए STFM प्रयोग असामान्य SOT के सबूत प्रकट करते हैं। PLD का उपयोग करके Si(111) सबस्ट्रेट पर एक अन्य वैन डर वाल्स सामग्री, GeTe, के  $\alpha$ -चरण की वृद्धि को अनुकूलित किया गया है। कोणीय-रिज़ॉल्व्ड STFM GeTe/ $\text{Ni}_{80}\text{Fe}_{20}$  उपकरणों में एक महत्वपूर्ण इन-प्लेन डंपिंग-लाइक टॉर्क को प्रकट करता है। गणना की गई डंपिंग-लाइक स्पिन टॉर्क कंडक्टिविटी  $(-1.25 \pm 0.11) \times 10^5 \hbar/2e \Omega^{-1}\text{m}^{-1}$  है, जो वैन डर वाल्स सामग्रियों के लिए रिपोर्ट की गई उच्चतम मूल्यों में से एक है। ये परिणाम वैन डर वाल्स सामग्रियों की अत्यधिक कुशल स्पिन्ट्रॉनिक्स उपकरणों के लिए क्षमता को रेखांकित करते हैं।

इसके बाद, हम गैर-सरेखित प्रतिचुंबक  $\text{Mn}_3\text{Sn}$  पर ध्यान केंद्रित करते हैं, जो एक मैग्नेटिक वाइल सेमीमेटल है और प्रभावी मेमोरी उपकरणों के लिए बड़ी संभावनाएँ रखता है। हम Ru को सीड लेयर के रूप में उपयोग करते हुए  $\text{Al}_2\text{O}_3$  सबस्ट्रेट पर उच्च-गुणवत्ता वाली एपिटैक्सियल c-प्लेन  $\text{Mn}_3\text{Sn}$  की वृद्धि करते हैं। c-प्लेन एपिटैक्सियल  $\text{Mn}_3\text{Sn}/\text{Ni}_{80}\text{Fe}_{20}$  पर स्पिन पंपिंग-प्रेरित इनवर्स स्पिन हॉल प्रभाव माप का उपयोग करके,  $\text{Mn}_3\text{Sn}$  पतली फिल्मों की स्पिन-डिफ्यूजन लंबाई ( $\lambda_{\text{Mn}_3\text{Sn}}$ ) और स्पिन हॉल कंडक्टिविटी ( $\sigma_{\text{SH}}$ )  $0.42 \pm 0.04 \text{ nm}$  और  $(-1.40 \pm 0.07) \times 10^5 \hbar/2e \Omega^{-1}\text{m}^{-1}$  मापी जाती हैं। जबकि  $\lambda_{\text{Mn}_3\text{Sn}}$  पहले के अध्ययन के अनुरूप है,  $\sigma_{\text{SH}}$  एक परिमाण के क्रम से अधिक है और विपरीत संकेत का है, जिसे फर्मी स्तर के परिवर्तन द्वारा समझाया गया है। a-प्लेन और बहुलकृष्णीय  $\text{Mn}_3\text{Sn}$  की वृद्धि को अनुकूलित किया गया है, जो विभिन्न क्रिस्टलीय उन्मुखियों में स्पिन-चार्ज रूपांतरण की तुलना

करने का अवसर प्रदान करता है।  $c$ -प्लेन और  $a$ -प्लेन उन्मुखियों के लिए स्पिन हॉल कोण लगभग समान है लेकिन विपरीत संकेत के हैं, संभवतः उनके कागोमे प्लेन की विभिन्न उन्मुखियों के कारण। इसके अतिरिक्त, एक व्यवस्थित STFM अध्ययन  $\text{Mn}_3\text{Sn}/\text{Py}$  उपकरणों में आउट-ऑफ-प्लेन ध्रुवीकृत स्पिन करंट ( $p_z$ ) की उपस्थिति को प्रकट करता है।  $c$ -प्लेन  $\text{Mn}_3\text{Sn}$  में  $p_z$  अनिसोट्रोपिक है, जबकि  $a$ -प्लेन  $\text{Mn}_3\text{Sn}$  में यह समदिश होता है। पहली बार  $a$ -प्लेन और बहुलकृष्णीय  $\text{Mn}_3\text{Sn}$  में असामान्य डंपिंग-लाइक और फील्ड-लाइक टॉर्क का अवलोकन किया गया है। ये परिणाम गैर-सरेखित प्रतिकुंबक  $\text{Mn}_3\text{Sn}$  को अगली पीढ़ी के स्पिंट्रॉनिक्स उपकरणों के लिए एक संभावित उम्मीदवार के रूप में प्रस्तुत करते हैं।

# Contents

<b>Certificate</b>	<b>i</b>
<b>Acknowledgements</b>	<b>iv</b>
<b>Abstract</b>	<b>vi</b>
<b>List of Figures</b>	<b>xiii</b>
<b>List of Tables</b>	<b>xxv</b>
<b>1 Fundamentals of spintronics</b>	<b>1</b>
1.1 Introduction: spintronics . . . . .	1
1.2 Basic concepts . . . . .	3
1.2.1 Interactions . . . . .	3
1.2.2 Giant magnetoresistance . . . . .	4
1.2.3 Spin current . . . . .	6
1.3 Magnetization dynamics . . . . .	7
1.4 Generation of spin current . . . . .	10
1.4.1 Spin pumping . . . . .	11
1.4.2 Spin Hall effect . . . . .	12

1.4.3	Magnetic spin Hall effect . . . . .	15
1.4.4	Rashba-Edelstein effect . . . . .	16
1.4.5	Unconventional spin current . . . . .	17
1.5	Detection of spin current . . . . .	18
1.5.1	Inverse spin Hall effect . . . . .	19
1.5.2	Inverse Rashba-Edelstein effect . . . . .	19
1.5.3	Spin torque ferromagnetic resonance . . . . .	20
1.6	Manipulation of magnetization using spin current . . . . .	22
1.6.1	Spin transfer torque . . . . .	22
1.6.2	Spin orbit torque . . . . .	23
1.7	Motivation of the thesis . . . . .	24
1.8	Thesis organization . . . . .	26
<b>2</b>	<b>Experimental techniques</b>	<b>29</b>
2.1	Sample preparation . . . . .	29
2.1.1	Sputtering . . . . .	30
2.1.2	Pulsed laser deposition . . . . .	32
2.1.3	Fabrication using photolithography . . . . .	33
2.1.4	Ion beam milling . . . . .	35
2.2	Characterization of thin films . . . . .	36
2.2.1	X-ray diffraction . . . . .	36
2.2.2	X-ray reflectivity . . . . .	38
2.2.3	Atomic force microscopy . . . . .	40

2.2.4	Magnetic force microscopy . . . . .	43
2.2.5	Piezo force microscopy . . . . .	43
2.2.6	Raman spectroscopy . . . . .	44
2.3	Static magnetic characterization . . . . .	46
2.3.1	Superconducting quantum interference device . . . . .	46
2.4	Dynamic magnetic characterization . . . . .	48
2.4.1	Ferromagnetic resonance . . . . .	48
2.4.2	Inverse spin Hall effect . . . . .	51
2.4.3	Spin torque ferromagnetic resonance . . . . .	52
<b>3</b>	<b>Large spin-to-charge conversion at the two-dimensional interface of transition metal dichalcogenides and permalloy</b>	<b>57</b>
3.1	Introduction . . . . .	57
3.2	Experimental details . . . . .	58
3.3	Results and discussion . . . . .	60
3.4	Conclusions . . . . .	71
<b>4</b>	<b>Optimization of growth of large-area SnS thin films and heterostructures for spin pumping and spin-orbit torque</b>	<b>73</b>
4.1	Introduction . . . . .	73
4.2	Experimental details . . . . .	74
4.3	Results and discussion . . . . .	76
4.4	Conclusions . . . . .	85
<b>5</b>	<b>Giant damping-like spin-torque conductivity in polycrystalline GeTe/Py heterostructures</b>	<b>87</b>

5.1	Introduction to GeTe	87
5.2	Experimental details	89
5.3	Results and discussion	89
5.4	Conclusions	96
<b>6</b>	<b>Large spin Hall conductivity in epitaxial thin films of kagome antiferromagnet Mn<sub>3</sub>Sn at room temperature</b>	<b>99</b>
6.1	Introduction	99
6.2	Experimental details	100
6.3	Results and discussion	101
6.4	Conclusions	107
<b>7</b>	<b>Crystalline orientation and Mn concentration dependent spin Hall effect in Mn<sub>3</sub>Sn</b>	<b>109</b>
7.1	Introduction	109
7.2	Experimental details	111
7.3	Results and discussion	112
7.4	Conclusions	120
<b>8</b>	<b>Non-trivial spin-orbit torques in non-collinear antiferromagnet Mn<sub>3</sub>Sn</b>	<b>121</b>
8.1	Introduction	121
8.2	Experimental details	122
8.3	Results and discussion	123
8.4	Conclusions	129
<b>9</b>	<b>Summary and outlook</b>	<b>131</b>
9.1	Summary of thesis	131

9.2 Outlook .....	134
<b>Bibliography</b>	<b>137</b>
<b>Publications</b>	<b>153</b>
<b>Biodata</b>	<b>157</b>



# List of Figures

1.1	(a) Magnetoresistance of a Fe/Cr multilayer (adapted from [4]). Schematics illustrating the GMR effect, displaying parallel alignment (b) and antiparallel alignment (d) of magnetic layers. Two-channel resistivity circuit for the parallel case (c) and antiparallel case (e).	5
1.2	Schematic illustration of (a) unpolarized charge current, (b) spin-polarized current, and (c) pure spin current. The unpolarized current consists of an equal number of up and down spin electrons, while the spin-polarized current predominantly contains one spin direction in the majority. A pure spin current exhibits no charge flow but maintains a finite flow of spin.	7
1.3	The motion of the magnetization unit vector $\mathbf{m}$ under the influence of (a) only the precessional term, (b) only the damping term, and (c) both the precessional and damping terms of the Landau-Lifshitz-Gilbert (LLG) equation.	9
1.4	Direction of different torques acting on the magnetization unit vector $\mathbf{m}$ under the influence of the LLGS equation, Eq. 1.15.	10
1.5	(a) Ferromagnetic resonance (FMR) condition in a single ferromagnetic (FM) layer and its (c) FMR spectrum. (b) Spin pumping from the FMR excited FM layer to the NM layer and its (d) FMR spectrum showing enhanced linewidth ( $\Delta H$ ) due to spin pumping.	11
1.6	Schematic illustrating the generation of pure spin current ( $J_S$ ) by an applied charge current ( $J_C$ ) due to spin Hall effect (SHE) in a heavy metal (HM) layer.	13

1.7	Schematic representing the parallel transport on a sphere. (a) Transport of a vector (orange arrow) from A through B, C, and finally back to A yields a vector different from the initial vector. The blue arrow represents the instantaneous normal vector to the surface. (b) The instantaneous state of different vectors at an infinitesimal area of the sphere. . . . .	14
1.8	Schematic representing (a) skew scattering and (b) side jump mechanisms responsible for extrinsic SHE. . . . .	15
1.9	An electron moving along the $x$ -direction with a momentum component of $k_x$ in the presence of a perpendicular electric field ( $E_z$ ) experiences a Rashba field ( $B_y$ ). . . . .	17
1.10	(a) A schematic energy dispersion curve split due to REE. (b) Fermi contours showing charge-to-spin conversion due to REE. (c) Fermi contours showing spin-to-charge conversion due to IREE. . . . .	18
1.11	Schematic illustrating the spin-pumping effect and the inverse spin-Hall effect (ISHE) in the FM/HM system. $J_S$ and $J_C$ represent the spatial directions of the spin current pumped from the FM layer by spin pumping and the electric current generated by ISHE, respectively. . . . .	20
1.12	Schematic illustrating SOT-driven FM magnetization ( $M$ ) dynamics in the ST-FMR measurements. $\tau_{\parallel}$ and $\tau_{\perp}$ are the in-plane and out-of-plane torques, respectively, generated by the RF current ( $I_{RF}$ ) along the $x$ -direction. $\varphi$ is the angle between the externally applied magnetic field ( $H$ ) and $I_{RF}$ , and $\theta_c$ is the cone angle of FM magnetization precession. . . . .	21
1.13	Schematic depicting the spin-transfer torque (STT) phenomenon. The black arrow represents the flow of electrons. Within the FM1 layer, red arrow depicts its magnetization direction. Similarly, inside the FM2 layer, the arrow represents the magnetization of FM2, on which the electrons exert a torque in the direction shown with the dotted black arrow. . . . .	23
1.14	Schematic showing the SOT phenomenon. $E_i$ represents the interfacial electric field due to the interfacial Rashba-Edelstein effect [67]. $\tau_{FL}$ and $\tau_{DL}$ denotes field-like and damping-like torque respectively. . . . .	24

1.15	Schematic illustrating SOT for three different spin polarization directions. In the diagram, $M$ represents the magnetization of the FM layer. $\tau_{\text{FL}}$ and $\tau_{\text{DL}}$ denotes field-like and damping-like torque, respectively. . . . .	25
2.1	(a) Schematic illustrating the process and various components of the sputtering system. (b) This schematic demonstrates how ions are trapped near the target surface by a magnetic field to enhance plasma formation. . . . .	31
2.2	AJA INTERNATIONAL, Inc. Orion 8 ultra-high vacuum magnetron sputtering system. . . . .	32
2.3	(a) Schematic showing the deposition process using the pulsed laser deposition (PLD) technique. (b) Image of the formation of a plume taken during the pulsed laser deposition of GeTe. . . . .	33
2.4	The device fabrication process using positive and negative photolithography. In positive photolithography, UV-exposed regions of the photoresist become more soluble, allowing for the removal of unwanted material. In negative photolithography, exposed areas become less soluble, preserving the desired pattern while removing unwanted material. . . . .	35
2.5	Schematic representation of ion beam milling process showing removal of target atoms (orange circles) from a sample surface due to bombardment of a beam of charged $\text{Ar}^+$ nuclei. . . . .	36
2.6	(a) This schematic portrays the diffraction of X-rays by a crystal. (b) Schematic illustrating the $\theta - 2\theta$ scan in the Bragg-Brentano geometry. $K_0$ and $K$ denote the wave vector of the incident and diffracted beam, respectively. . . . .	38
2.7	The schematic illustrates the grazing incidence X-ray diffraction (GIXRD) setup. In this setup, the incident angle ( $\alpha$ ) is kept constant, typically at just a few degrees or even less. The detector is rotated, and the intensity is recorded at various scattering angles. . . . .	39
2.8	In the X-ray reflectometry (XRR) setup, as schematically illustrated in (a), an incident X-ray at an angle ( $\theta$ ) greater than the critical angle ( $\theta_c$ ) enters the thin films. The alteration in refractive index at the interface induces oscillations in the reflective X-rays, as depicted in (b) by typical XRR scan data. . . . .	40

2.9	Schematic of atomic force microscopy (AFM) operation where a tip attached to a cantilever is scanned over the sample's surface to map the contours of a sample. . . . .	41
2.10	The behavior of the force between the tip and the sample as a function of the tip-sample distance, illustrating various AFM operating modes. In the figure, different operating regimes are represented by different colors: pink signifies the contact mode, green represents the tapping mode, and orange is indicative of the non-contact mode. . . . .	42
2.11	A schematic illustration of the Rayleigh and Raman scattering processes is presented. The blue arrow represents excitation induced by laser light. The green and red arrows represent the Stokes and anti-Stokes scattering processes, respectively. Dashed lines depict the virtual state. . . . .	45
2.12	The schematic depicts a Raman spectrometer setup with a laser light source interacting with the sample. . . . .	46
2.13	The schematic depicts the construction and operating principle of the SQUID. Two Josephson junctions are arranged in a superconducting ring, forming the SQUID. . . . .	47
2.14	Schematic of a co-planar waveguide (CPW)-based broadband FMR setup. The setup comprises a signal generator as an RF source connected to the input port of the CPW. The transmitted signal is detected by a microwave diode and a lock-in amplifier. The sweeping static field is generated by an electromagnet and modulated with small frequency sine waves to provide a reference signal to the lock-in amplifier. . . . .	49
2.15	Cross-sectional view of a CPW with a sample on top. The figure also shows the applied RF magnetic field, which is transverse to the DC magnetic field. . . . .	50
2.16	(a) Measured FMR spectra for the Py(8 nm)/Al(3 nm) sample at varying frequencies ( $f$ ) from 4-16 GHz, where the measured signal is fitted with a derivative Lorentzian equation. (b) The linewidth ( $\Delta H$ ) variation vs. $f$ is linearly fitted for calculating Gilbert damping ( $\alpha_{\text{eff}}$ ). (c) $f$ vs. resonance field ( $H_r$ ) fitted using Kittel's formula to determine the effective saturation magnetization ( $M_{\text{eff}}$ ). . . . .	51
2.17	(a) Modified CPW with copper pads affixed to each side of the signal line for ISHE measurements. (b) Measured ISHE voltage (open circle) for a Py(8 nm)/Ta(5 nm) sample fitted with Eq. 2.6 to extract symmetric and antisymmetric components. . . . .	52

2.18	Schematic of ST-FMR measurements with a projected field vector magnet, which enables systematic angular-dependent studies. Angular measurements discussed in the thesis are conducted using a programmable motor-based rotating stage. . . . .	53
2.19	(a) ST-FMR signal ( $V_{\text{mix}}$ ) for Pt(5 nm)/Py(10 nm)/AlO <sub>x</sub> (2 nm) sample fitted with Eq. 2.7 to separate symmetric $V_S$ (green) and antisymmetric $V_A$ (blue) parts. The corresponding angular dependence of (b) $V_S$ and (c) $V_A$ components, fitted with Eqs. 2.8 and 2.9, respectively. (d) ST-FMR signal ( $V_{\text{mix}}$ ) for GeTe(15 nm)/Py(8 nm)/AlO <sub>x</sub> (2 nm) sample fitted with Eq. 2.7 to separate symmetric $V_S$ (green) and antisymmetric $V_A$ (blue) parts. The corresponding angular dependence of (e) $V_S$ and (f) $V_A$ components, fitted with Eqs. 2.8 and 2.9, respectively. . . . .	55
3.1	(a) Schematic illustration of spin splitting in the valence band around the $K$ -point of MoX <sub>2</sub> and WX <sub>2</sub> ML TMDs. Here, X denotes S or Se. (b) Theoretical spin splitting of the uppermost valence band at the $K$ -point for different ML TMDs [116]. (c) The ML TMD/FM structure used in this work is depicted schematically, illustrating how spin current is injected via spin pumping. . . . .	59
3.2	(a)-(d) Raman spectra for different ML TMDs before (open triangles) and after the deposition of Py(10 nm) and Ta (3 nm) layers (open circles) (a) MoS <sub>2</sub> , (b) MoSe <sub>2</sub> , (c) WS <sub>2</sub> , and (d) WSe <sub>2</sub> , respectively. . . . .	61
3.3	Raman spectra at 8 different points for ML (a) MoS <sub>2</sub> and (d) WS <sub>2</sub> . The peak position difference between A <sub>1g</sub> and E <sub>2g</sub> <sup>1</sup> peaks for ML (b) MoS <sub>2</sub> and (e) WS <sub>2</sub> . Trend of intensity for ML (c) MoS <sub>2</sub> and (f) to confirm uniformity of the TMDs. . . . .	61
3.4	Raman spectra at 8 different points for ML (a) MoSe <sub>2</sub> and (c) WSe <sub>2</sub> . Trend of intensity for ML (b) MoSe <sub>2</sub> and (d) WSe <sub>2</sub> to confirm uniformity of the TMDs. . . . .	62
3.5	AFM images of (a) reference Py(10 nm)/Ta(3 nm), (b) ML MoS <sub>2</sub> /Py(10 nm)/Ta(3 nm), (c) ML MoSe <sub>2</sub> /Py(10 nm)/Ta(3 nm), (d) ML WS <sub>2</sub> /Py(10 nm)/Ta(3 nm), (e) ML WSe <sub>2</sub> /Py(10 nm)/Ta(3 nm) samples respectively. All the samples have similar morphology and roughness as they are prepared simultaneously inside a sputtering chamber. . . . .	63

3.6	Field dependence of FMR (top row) and corresponding $I_C$ derived from IREE measurements (middle and bottom row) for (a) Py(10 nm)/Ta(3 nm), (b) ML MoS <sub>2</sub> /Py(10 nm)/Ta(3 nm), (c) ML MoSe <sub>2</sub> /Py(10 nm)/Ta(3 nm), (d) ML WS <sub>2</sub> /Py(10 nm)/Ta(3 nm), (e) ML WSe <sub>2</sub> /Py(10 nm)/Ta(3 nm) samples. Here, numbers in parenthesis reflect thickness in nanometers and ML is abbreviation for monolayer. The middle row is for $H > 0$ while the bottom row is for $H < 0$ . The solid lines in middle and bottom row are fits to experimental data. . . . .	64
3.7	Measured $I_C$ in Py(x)/SiO <sub>2</sub> (3 nm) for two different thicknesses (x) of Py layer. . .	65
3.8	Measured $I_C$ for ML MoS <sub>2</sub> /Cu(5 nm)/Py(10 nm)/Ta(3 nm) (Red symbols) and Cu(5 nm)/Py(10 nm)/Ta(3 nm) (black symbols). . . . .	66
3.9	Plot of $I_C$ for Py (10 nm) samples having different capping layers, namely, Pt, Ta, and SiO <sub>2</sub> . . . . .	67
3.10	Measured $I_C$ for CFB (10 nm)/Al (3 nm) (black) and MoS <sub>2</sub> (ML)/CFB (10 nm)/Al (3 nm) (red). The measurement conditions were kept identical with Fig. 3.6. . . .	67
3.11	(a) The extracted data (symbols) for $\Delta H$ versus $f$ and its fit to Eq. 3.3 (solid line). (b) The plot of $\Delta H_0$ extracted from the fit in Fig. 3.11 (a). (c) Plot of $ j_C^{TMD/Py} $ and $j_s$ for various ML TMDs/Py(10 nm)/Ta(3 nm) samples, which follows the trend of SOC strength shown in Fig. 3.1 (b). (d) $f$ vs. $H_r$ data (points) fitted with Kittel's formula (solid lines) to extract $M_{\text{eff}}$ . (e) Magnetization curves for various ML TMD/Py samples measured using VSM. (f) Comparative plot of $M_{\text{eff}}$ (green axis) and $M_S$ values (brown axis) showing that the magnetic properties of Py are similar for all ML TMD/Py(10 nm)/Ta(3 nm) samples. . . . .	69
3.12	Comparative plot of $\lambda_{\text{IREE}}$ for different Rashba interfaces. . . . .	70
4.1	(a) A schematic side view of the structure of bilayer SnS. (b) X-ray diffraction (XRD) data for SnS thin film grown at various substrate temperatures ( $T_S$ ). (c) X-ray reflectivity (XRR) data and corresponding fits (solid line) for samples deposited at 473 K (open circle) and room temperature, 300 K (open triangle). Acquired Raman spectra for samples grown at (d) 473 K and (e) 300 K with different thicknesses. (f) Raman spectra at ten different spots on the same large area SnS thin film of thickness 5.4 nm. . . . .	77

4.2	Atomic force microscopy (AFM) images of (a) reference Py(8 nm)/AlO <sub>x</sub> (3 nm), and SnS( <i>t</i> <sub>SnS</sub> )/Py(8 nm)/AlO <sub>x</sub> (3 nm), where <i>t</i> <sub>SnS</sub> is (b) 0.4, (c) 0.8 (d) 1.2, (e) 1.6, (f) 2.0, (g) 2.4, (h) 3.2, (i) 4.0, (j) 4.8, (k) 5.6, (l) 6.4, and (m) 8 nm, respectively. Here, SnS was deposited at 473 K. . . . .	78
4.3	Atomic force microscopy (AFM) images of (a) reference Py(8 nm)/AlO <sub>x</sub> (3 nm), and SnS( <i>t</i> <sub>SnS</sub> )/Py(8 nm)/AlO <sub>x</sub> (3 nm), where <i>t</i> <sub>SnS</sub> is (b) 0.7, (c) 1.4 (d) 2.0, (e) 2.7, (f) 3.4, (g) 4.0, (h) 4.7, and (i) 5.4 nm, respectively. Here, SnS was deposited at 300 K. . . . .	79
4.4	(a) The trend of RMS roughness of SnS thin films deposited at 300 K and 473 K. The roughness is determined from the AFM scans as a function of film thickness ( <i>t</i> <sub>SnS</sub> ). Scanning electron microscopy (SEM) images for 4 nm SnS samples deposited at (b) 300 K and (c) 473 K showing smooth and island-type growth, respectively. . .	79
4.5	(a) XPS survey spectrum of SnS sample deposited at 300 K. (b) High-resolution XPS spectrum and its fit showing peaks of Sn 3d binding energies at 486.0 and 494.3 eV. (c) High-resolution deconvoluted XPS spectrum and its fit showing peaks of S 2p binding energies at 161.3 and 162.6 eV. . . . .	80
4.6	(a) AFM topography near a SnS step. (b) Lateral PFM response showing the contrast between substrate and SnS. . . . .	80
4.7	(a) EDX spectrum of Sn, S, Si and O in SnS thin film deposited at RT. (b), (c) Energy-dispersive X-ray spectroscopy (EDX) maps for Sn and S, respectively, showing a homogeneous distribution of both the elements. . . . .	81
4.8	(a) IV measurements for SnS(4 nm) and Py(8 nm) samples using the four-probe method. The slope of both the curve hints at a much higher resistivity of SnS compared to Py. (b) Raman measurements before (only SnS layer) and after Py deposition (SnS/Py) showing the vibration modes from SnS. The peak positions of the Raman spectra obtained after the deposition of Py coincide well with their corresponding pristine SnS thin film. . . . .	82

4.9	(a) Linewidth ( $\Delta H$ ) as a function of RF frequency ( $f$ ) for SnS(4 nm) samples deposited at 473 K (open circle) and 300 K (open triangle) with Py(8 nm)/AlO <sub>x</sub> (3 nm) on top. (b) $f$ vs. resonance field ( $H_r$ ) plot with their corresponding best fit (solid line) using Eq. 4.2. Variation of (c) inhomogeneous line broadening ( $\Delta H_0$ ), and (d) effective saturation magnetization ( $4\pi M_{\text{eff}}$ ) as a function of $t_{\text{SnS}}$ . The trend of effective Gilbert damping parameter ( $\alpha_{\text{eff}}$ ) and uniaxial anisotropy field ( $H_k$ ) as a function of $t_{\text{SnS}}$ for sample deposited at (e) 473 K and (f) 300 K. . . . .	83
4.10	(a) Schematic illustrating STFM measurements setup and SnS/Py bilayer microstrip device with in-plane ( $\tau_{\parallel}$ ) and out-of-plane ( $\tau_{\perp}$ ) torque generated by the electric current along $x$ -direction. (b)-(c) Scanning electron microscopy (SEM) image of the STFM device. (d) The STFM spectra (open symbols) of SnS(1.3 nm)/Py(8 nm) sample at 5 GHz frequency, where red and blue dotted curves represent the symmetric ( $V_S$ ) and anti-symmetric ( $V_A$ ) components of the rectified voltage, respectively. (e), (f) The angular dependence of $V_S$ and $V_A$ components, respectively. . . . .	84
5.1	(a) Crystal structure of $\alpha$ -GeTe having rhombohedral structure ( $R3m$ ). The structure was generated using VESTA [177]. (b) ARPES data shows well-resolved Rashba-split bulk bands, which allowed to derive the momentum splitting $\Delta k_R \approx 0.13 \text{ \AA}^{-1}$ and Rashba parameter $\alpha_R$ to be around $4.2 \text{ eV \AA}$ . ARPES data is adapted from [178]. . . . .	88
5.2	(a)–(c) The depth profiled x-ray photoelectron spectroscopy (XPS) spectra of Ge, Te, and Si, respectively, for <i>uncapped</i> GeTe thin film. The numbers with the curve represent the etching depth in nanometers. The inset in (b) provides a zoomed plot of the unetched spectrum for clarity. The spectra show that the GeTe thin film gets oxidized up to $\sim 7.2 \text{ nm}$ if not capped. . . . .	90
5.3	(a)-(c) The XPS spectra of Ge, Te, and Si, respectively, for GeTe(23 nm) thin film capped with Al(3 nm). The spectra show that the Al capping has protected the GeTe film from getting oxidized. . . . .	90

5.4	(a) Grazing incidence XRD pattern of 23 nm-thick GeTe thin film. The observed peaks match well with the $\alpha$ -phase of GeTe. Inset: IV measurements for Py(8 nm) (green) and GeTe(15 nm) (red) samples using the four-probe method. (b) The room temperature Raman spectra before (black) and after (red) deposition of Py on top of GeTe show both E and $A_1$ modes at 88.3 and 125.6 $\text{cm}^{-1}$ . (c) AFM image of GeTe thin film showing a smooth surface with RMS roughness < 0.2 nm. . . . .	91
5.5	(a) SEM image of the STFMR device. (b) The schematic depicts the setup for STFMR measurements and a microstrip device consisting of a GeTe(15 nm)/Py(8 nm)/AlO <sub>x</sub> (2 nm) bilayer. This device is subject to electric current flowing along the $x$ -direction, resulting in the generation of both in-plane ( $\tau_{\parallel}$ ) and out-of-plane ( $\tau_{\perp}$ ) torque. (c) STFMR spectra at 6 GHz frequency for Py (green) and GeTe/Py (red) samples. (d) linewidth ( $\Delta H$ ) vs. frequency ( $f$ ) (open circle) and their corresponding fit (solid lines) with Eq. 5.2. (e) $f$ vs. $H_r$ curve for different $t_{\text{Mn}_3\text{Sn}}$ (open circle) and their corresponding fit (solid lines) with Eq. 5.3. . . . .	93
5.6	The angular dependence of (a) symmetric ( $V_S$ ) and (b) antisymmetric ( $V_A$ ) component, respectively for the GeTe(15 nm)/Py(8 nm)/AlO <sub>x</sub> (2 nm) sample. . . . .	94
5.7	(a) Plot of spin-torque conductivities ( $\sigma_{\text{DL}}^y$ , $\sigma_{\text{FL}}^z$ , and $\sigma_{\text{DL}}^z$ ) for reference Py(8 nm)/AlO <sub>x</sub> (2 nm) and GeTe(15 nm)/Py(8 nm)/AlO <sub>x</sub> (2 nm) samples. The spin-torque conductivities for the Py sample are multiplied by a factor of 10 to enhance the visibility of the spin-torque conductivities in the plot. (b) Comparative plot of spin torque conductivity $\sigma_{\text{DL}}^y$ for other van der Waals materials (MoS <sub>2</sub> [188], MoTe <sub>2</sub> [187], WTe <sub>2</sub> [50], NbSe <sub>2</sub> [171], PtTe <sub>2</sub> [189]) with $\alpha$ -GeTe investigated in this work. . . . .	96
6.1	(a) The magnetic and crystal structure of $c$ -plane Mn <sub>3</sub> Sn, revealing the kagome lattice of Mn magnetic moments. (b) Measured X-ray reflectivity (red circles) for the Ru(7 nm)/Mn <sub>3</sub> Sn(30 nm)/AlO <sub>x</sub> (2 nm) thin film and corresponding theoretical fit (black solid line). (c) The surface topography measured using AFM. The scan area is 2 $\mu\text{m} \times 2 \mu\text{m}$ . (d) X-ray diffraction (XRD) spectra for the Ru(7 nm)/Mn <sub>3</sub> Sn(30 nm)/AlO <sub>x</sub> (2 nm) thin film. (e) Comparative XRD data for 30 nm (wine) and 10 nm (blue) Mn <sub>3</sub> Sn samples. (f) The corresponding $\varphi$ -scan for Al <sub>2</sub> O <sub>3</sub> ( $11\bar{2}3$ ) (violet), Ru ( $10\bar{1}1$ ) (cyan) and Mn <sub>3</sub> Sn ( $20\bar{2}1$ ) (wine). . . . .	102

6.2	EDX spectrum of (a) $\text{Al}_2\text{O}_3/\text{Ru}(7\text{ nm})/\text{Mn}_3\text{Sn}(10\text{ nm})/\text{NiFe}(8\text{ nm})/\text{AlO}_x(3\text{ nm})$ and (b) $\text{Al}_2\text{O}_3/\text{Ru}(7\text{ nm})/\text{Mn}_3\text{Sn}(30\text{ nm})/\text{AlO}_x(3\text{ nm})$ samples. . . . .	103
6.3	Elements distribution maps for (a) Mn and (b) Sn measured using electron probe microanalyzer (EPMA). (c) SQUID magnetization ( $M$ ) curve of $\text{Mn}_3\text{Sn}$ (30 nm) sample. Inset: Magnetization ( $M$ ) curve of $\text{Mn}_3\text{Sn}$ (30 nm)/Py (8 nm) bilayer thin film. . . . .	104
6.4	(a) The measured FMR signal at 4 GHz for samples ( $\text{Al}_2\text{O}_3/\text{Ru}(7\text{ nm})/\text{Mn}_3\text{Sn}(t_{\text{Mn}_3\text{Sn}})/\text{Py}(8\text{ nm})/\text{AlO}_x(2\text{ nm})$ ) having different thickness, $t_{\text{Mn}_3\text{Sn}}$ of $\text{Mn}_3\text{Sn}$ near the resonance field ( $H_r$ ). (b) linewidth ( $\Delta H$ ) vs. frequency ( $f$ ) (open circle) and their corresponding fit (solid lines) with Eq. 6.1. (c) $f$ vs. $H_r$ curve for different $t_{\text{Mn}_3\text{Sn}}$ (open circle) and their corresponding fit (solid lines) with Eq. 6.2. . . . .	105
6.5	(a) A representative ISHE signal for $\text{Mn}_3\text{Sn}(10\text{ nm})/\text{Py}(8\text{ nm})/\text{AlO}_x(2\text{ nm})$ sample. Inset: ISHE signal for a reference Ta(5 nm)/Py(8 nm) bilayer to establish the negative sign of spin Hall conductivity ( $\sigma_{\text{SH}}$ ) in $\text{Mn}_3\text{Sn}(10\text{ nm})$ (b) The plot of the ratio $V_{\text{ISHE}}^{\text{sym}}/Rw$ as a function of $\text{Mn}_3\text{Sn}$ thickness ( $t_{\text{Mn}_3\text{Sn}}$ ) and its fit with Eq. 6.4 to determine $\lambda_{\text{Mn}_3\text{Sn}}$ and $\theta_{\text{SH}}$ . The inset depicts the predicted $\sigma_{\text{SH}}$ based on Ref. [195], when the Fermi level is moved upward with electron doping <i>e.g.</i> , due to high Mn concentration. . . . .	106
7.1	(a) Crystallographic hexagonal structure of $\text{Mn}_3\text{Sn}$ . Mn atoms are depicted in blue, and Sn atoms are shown in yellow. (b) The magnetic texture of $\text{Mn}_3\text{Sn}$ reveals the inverse triangular spin structure of Mn magnetic moments, represented by the red arrows. The bigger orange arrow represents the ferroic ordering of a cluster magnetic octupole ( $m_{\text{oct}}$ ). (c) Schematic illustration of the $c$ -plane (orange) and $a$ -plane (pink) of $\text{Mn}_3\text{Sn}$ . For the $c$ -plane ( $a$ -plane) film, the Kagome lattice is in (out of) the film plane. The above structures were generated using VESTA [177].	110
7.2	(a) Brillouin zone of $\text{Mn}_3\text{Sn}$ showing the distribution of Weyl points near the Fermi level. (b) Band structure along high symmetry points for $\text{Mn}_3\text{Sn}$ . (c) ARPES results for $\text{Mn}_3\text{Sn}$ with different Mn concentrations show a shift in the Fermi level. The figures are adapted from [219]. . . . .	111

7.3	(a) $a$ -plane $\text{Mn}_3\text{Sn}$ films on $r$ -sapphire substrate deposited at 420 °C and post annealed at 650 °C for 1 hr, and its (b) corresponding atomic force microscopy (AFM) image of 60 nm thick $a$ -plane $\text{Mn}_3\text{Sn}$ having very large RMS roughness of around 3.8 nm. . . . .	113
7.4	XRD patterns are presented for: (a) $c$ -plane $\text{Mn}_3\text{Sn}$ films on $c$ -sapphire substrate, (b) $a$ -plane $\text{Mn}_3\text{Sn}$ films on $r$ -sapphire substrate, and (c) polycrystalline $\text{Mn}_3\text{Sn}$ thin films on $\text{Si}/\text{SiO}_2$ substrates. The thickness of $\text{Mn}_3\text{Sn}$ is 60 nm in all cases. . .	113
7.5	AFM images of 60 nm thick (a) $c$ -plane $\text{Mn}_3\text{Sn}$ , (b) $a$ -plane $\text{Mn}_3\text{Sn}$ , and (c) polycrystalline $\text{Mn}_3\text{Sn}$ film surfaces and their corresponding magnetic force microscopy (MFM) images on the same scan area in the second row. The scan area is $3 \times 3 \mu\text{m}^2$ and the scale bar is 600 nm. . . . .	114
7.6	(a) The out-of-plane magnetic hysteresis loop ( $M-H_z$ ) for (a) $a$ -plane $\text{Mn}_3\text{Sn}$ and (b) polycrystalline $\text{Mn}_3\text{Sn}$ . All the measurements were done at room temperature. . .	115
7.7	The longitudinal current ( $I$ ) versus voltage ( $V$ ) data (red circles) for (a) $\text{Ru}(7 \text{ nm})/c\text{-Mn}_3\text{Sn}(60 \text{ nm})/\text{AlO}_x(1.5 \text{ nm})$ , (b) $\text{Ru}(7 \text{ nm})/\text{AlO}_x(1.5 \text{ nm})$ , and (c) $a\text{-Mn}_3\text{Sn}(60 \text{ nm})/\text{AlO}_x(1.5 \text{ nm})$ used to calculate the resistivity of $\text{Mn}_3\text{Sn}$ and Ru. Inset in (a) shows an optical image of the fabricated Hall bar. . . . .	116
7.8	A representative FMR (a) and its corresponding ISHE (b) signal for $a$ -plane $\text{Mn}_3\text{Sn}(60 \text{ nm})/\text{Py}(8 \text{ nm})/\text{AlO}_x(2 \text{ nm})$ sample performed at 3 GHz frequency. . .	116
7.9	(a) The trend of effective saturation magnetization ( $M_{\text{eff}}$ ) and inhomogeneous line broadening ( $\Delta H_0$ ) with $a$ -plane $\text{Mn}_3\text{Sn}$ thickness ( $t_{\text{Mn}_3\text{Sn}}$ ). The trend of (b) effective spin mixing conductance ( $g_{\uparrow\downarrow}$ ), $\Delta V_{\text{ISHE}}^{\text{sym}}/Rw$ , and (c) spin Hall conductivity ( $\sigma_{\text{SH}}$ ) as a function of $t_{\text{Mn}_3\text{Sn}}$ . The variation of $M_{\text{eff}}$ and $\Delta H_0$ with the introduction of 2 nm Al spacer layer. The trend of (e) $g_{\uparrow\downarrow}$ , $V_{\text{ISHE}}^{\text{sym}}/Rw$ , and (f) $\sigma_{\text{SH}}$ with and without 2 nm Al spacer between $\text{Mn}_3\text{Sn}$ and $\text{Py}(8 \text{ nm})/\text{AlO}_x(2 \text{ nm})$ . The dotted line shows the average value of $\sigma_{\text{SH}}$ . . . . .	118
7.10	(a) The variation of $M_{\text{eff}}$ and $\Delta H_0$ with the Mn atomic concentration in $a$ -plane $\text{Mn}_3\text{Sn}$ . The trend of (b) $g_{\uparrow\downarrow}$ , $\Delta V_{\text{ISHE}}^{\text{sym}}/Rw$ , and (c) $\sigma_{\text{SH}}$ as a function of Mn atomic concentration for $a\text{-Mn}_3\text{Sn}(60 \text{ nm})/\text{Py}(8 \text{ nm})/\text{AlO}_x(2 \text{ nm})$ sample. . . . .	119

- 7.1.1 (a)-(b) Schematic illustrating that the kagome plane is in the in-plane (out-of-plane) direction of the  $c$ -plane ( $a$ -plane) oriented  $\text{Mn}_3\text{Sn}(60 \text{ nm})/\text{Py}(8 \text{ nm})/\text{AlO}_x(2 \text{ nm})$  thin films. (c) The variation of  $M_{\text{eff}}$  and  $\Delta H_0$  with the crystal orientation. The trend of (d)  $g_{\uparrow\downarrow}$ ,  $\Delta V_{\text{ISHE}}^{\text{sym}}/Rw$ , and (e)  $\sigma_{\text{SH}}$  with different crystal orientation of  $\text{Mn}_3\text{Sn}$ . . . . . 120
- 8.1 (a) SEM image of the STFMR device. (b) The schematic depicts the setup for STFMR measurements and a microstrip device consisting of a  $\text{Ru}(7 \text{ nm})/c\text{-Mn}_3\text{Sn}(10 \text{ nm})/\text{Py}(8 \text{ nm})/\text{AlO}_x(2 \text{ nm})$  bilayer. This device is subject to electric current flowing along the  $[2\bar{1}\bar{1}0]$ -direction, resulting in the generation of both in-plane ( $\tau_{\parallel}$ ) and out-of-plane ( $\tau_{\perp}$ ) torque. (c)-(f) STFMR mixing voltage ( $V_{\text{mix}}$ ) at in-plane magnetic field angles  $\varphi = 40^\circ, 150^\circ, 220^\circ$  and  $330^\circ$ , respectively. The red curve is the best fit to the data with Eq. 8.1. The green and blue curves are the antisymmetric ( $V_A$ ) and symmetric ( $V_S$ ) components, respectively. . . . . 124
- 8.2 (a) Schematic illustration of in-plane damping-like torque  $\tau_{\text{DL}}^y$  and out-of-plane field-like torque  $\tau_{\text{FL}}^y$  for originating due to in-plane polarized spin current ( $p_y$ ) when  $I_{\text{RF}} \perp m_{\text{oct}}$ . Symmetric (b) and anti-symmetric (c) components of the STFMR signal for  $I_{\text{RF}} \perp m_{\text{oct}}$ . (d) Schematic illustrating an unconventional in-plane field-like torque  $\tau_{\text{FL}}^z$  originating from out-of-plane polarized spin current ( $p_z$ ) when  $I_{\text{RF}} \parallel m_{\text{oct}}$ . Symmetric (e) and anti-symmetric (f) components of the STFMR signal for  $I_{\text{RF}} \parallel m_{\text{oct}}$ . The above measurements are for  $\text{Ru}(7 \text{ nm})/c\text{-Mn}_3\text{Sn}(10 \text{ nm})/\text{Py}(8 \text{ nm})/\text{AlO}_x(2 \text{ nm})$  devices. . . . . 125
- 8.3 (a) Schematic illustrating the torques present when  $m_{\text{oct}}$  is tilted in the out-of-plane direction for  $a$ -plane oriented  $\text{Mn}_3\text{Sn}(60 \text{ nm})/\text{Py}(8 \text{ nm})/\text{AlO}_x(2 \text{ nm})$ .  $V_S$  (b) and  $V_A$  (c) components as a function of angle  $\varphi$  for  $a$ -plane  $\text{Mn}_3\text{Sn}/\text{Py}$  bilayer. (d) Schematic illustrating the torques present when  $m_{\text{oct}}$  is in both in-plane and out-of-plane directions for polycrystalline  $\text{Mn}_3\text{Sn}$ .  $V_S$  (e) and  $V_A$  (f) components for polycrystalline  $\text{Mn}_3\text{Sn}/\text{Py}$  bilayer showing the presence of  $p_z$ . . . . . 126
- 8.4 Anti-symmetric ( $V_A$ ) and symmetric ( $V_S$ ) components of STFMR signal for various angles ( $\theta_a$ ) with respect to the crystallographic direction  $[0001]$  for  $a\text{-Mn}_3\text{Sn}(60 \text{ nm})/\text{Py}(8 \text{ nm})/\text{AlO}_x(2 \text{ nm})$ . . . . . 127

8.5	Anti-symmetric (top row) and symmetric (bottom row) components of STFM signal for $I_{\text{RF}} \parallel m_{\text{oct}}$ as a function of $\text{Mn}_3\text{Sn}$ thickness ( $t_{\text{Mn}_3\text{Sn}}$ ) for $c\text{-Mn}_3\text{Sn}(t_{\text{Mn}_3\text{Sn}})/\text{Py}(8\text{ nm})/\text{AlO}_x(2\text{ nm})$ . $V_A$ follows a conventional $\sin(2\varphi)\cos(\varphi)$ dependence whereas $V_S$ has an additional $\sin(2\varphi)$ dependence. . . . .	128
8.6	(a) Summary of unconventional field-like torque $\tau_{\text{FL}}^z/\tau_{\text{FL}}^y$ and (b) damping-like torque $\tau_{\text{DL}}^z/\tau_{\text{FL}}^y$ ratios as functions of the crystallographic angle ( $\theta_a$ ) in $a\text{-Mn}_3\text{Sn}(60\text{ nm})/\text{Py}(8\text{ nm})/\text{AlO}_x(2\text{ nm})$ samples. $\theta_a$ is the angle between $I_{\text{RF}}$ and the crystallographic direction [0001] for $a\text{-Mn}_3\text{Sn}$ . (c) The trend of normalized torque $\tau_{\text{FL}}^z/\tau_{\text{FL}}^y$ as a function of $c\text{-Mn}_3\text{Sn}$ thickness ( $t_{\text{Mn}_3\text{Sn}}$ ) for the $c\text{-Mn}_3\text{Sn}(t_{\text{Mn}_3\text{Sn}})/\text{Py}(8\text{ nm})/\text{AlO}_x(2\text{ nm})$ sample stack. (d) The crystal orientation dependence on different torques shows that the conventional torque remains nearly constant, whereas the unconventional torque is dependent on crystal orientation. . . . .	129



# List of Tables

2.1	Dependence of symmetric ( $V_S$ ) and antisymmetric ( $V_A$ ) components on the angle $\varphi$ between applied current and FM magnetization ( $\hat{m}$ ) for spin polarization in the $x$ -, $y$ -, and $z$ -directions. The first set of three entries pertains to the DL (Damping-Like Torque) components, while the last three entries describe the FL (Field-Like Torque) components. The parentheses in the torque notation indicate whether the torque is in-plane (IP) or out-of-plane (OOP), considering $\hat{m}$ to be in-plane. Conventional and unconventional torques are highlighted in blue and purple, respectively. . . . .	56
3.1	Values of effective damping parameter subtracted from reference sample ( $\Delta\alpha_{\text{eff}}$ ), spin mixing conductance ( $g_{\uparrow\downarrow}$ ), charge current density ( $j_C$ ), spin current density ( $j_S$ ), Rashba efficiency parameter ( $\lambda_{\text{REE}}$ ), pseudo spin Hall angle ( $\theta_{\text{PSH}}$ ). . . . .	71
9.1	Comparison of the magnitude of spin Hall conductivity ( $\sigma_{\text{SH}}$ ) for three different classes of materials: heavy metals, van der Waals materials, and non-collinear antiferromagnets. . . . .	132

